JOURNAL OF PROPULSION AND POWER
Vol. 26, No. 3, May–June 2010

Multiphysics Computational Analysis of a Solid-Core Nuclear Thermal Engine Thrust Chamber

Ten-See Wang* and Francisco Canabal†
NASA Marshall Space Flight Center, Huntsville, Alabama 35812
Yen-Sen Chen‡
Engineering Sciences, Inc., Huntsville, Alabama 35815
and
Gary Cheng§
University of Alabama at Birmingham, Birmingham, Alabama 35294

DOI: 10.2514/1.47759

The objective of this effort is to develop an efficient and accurate computational fluid dynamics and heat transfer methodology to predict thermal, fluid, and hydrogen environments of a hypothetical solid-core nuclear thermal engine: the small engine. Several theoretical power profiles were imposed on the solid core to represent the effect of nuclear heating, and their effects on hydrogen conversion, heat transfer efficiency, and thrust performance were investigated and reported. The computational methodology is based on an unstructured-grid, pressure-based, all speeds, chemically reacting, computational fluid dynamics and heat transfer platform, and formulations of flow and heat transfer through porous media were implemented to describe those of thousands of flow channels inside the solid core. In addition, formulations of conjugate heat transfer were implemented in a previous study to describe the heat transfer between other supporting solid components and the working fluid. The computational domain covers the entire thrust chamber so that the heat transfer effects impact the thrust performance directly. The result shows that the computed core-exit gas temperature, specific impulse, and core pressure drop agree well with those of the small engine. Finite rate chemistry is found to be very important in predicting the proper energy balance, because naturally occurring hydrogen decomposition is endothermic. Locally strong hydrogen conversion associated with centralized power profile gives poor heat transfer efficiency and lower thrust performance. On the other hand, uniform hydrogen conversion associated with a more uniform radial power profile achieves higher heat transfer efficiency and higher thrust performance.

Nomenclature

C_1, C_2, C_3, C_μ	=	turbulence modeling constants (1.15, 1.9, 0.25, and 0.09)
C_p	=	heat capacity
D	=	diffusivity
d	=	flow channel diameter
f_L, f_q	=	empirical multipliers
H	=	total enthalpy
K	=	thermal conductivity
k	=	turbulent kinetic energy
L	=	drag loss due to porous media
p	=	pressure
Q	=	volumetric heat source
Re	=	Reynolds number
T	=	temperature
t	=	time, s
U	=	flow speed
u_i	=	mean velocities in three directions
x	=	Cartesian coordinates
α	=	species mass fraction
β	=	porosity or void of fraction
ε	=	turbulent kinetic energy dissipation rate
μ	=	viscosity
μ_t	=	turbulent eddy viscosity, $\rho C_\mu k^2/\varepsilon$
Π	=	turbulent kinetic energy production
ρ	=	density
σ	=	turbulence modeling constants
τ	=	shear stress
ω	=	chemical species production rate

Subscripts

g	=	gas
p	=	nuclear power source
r	=	radiation
s	=	surface, solid, or porous media
t	=	turbulent flow

Presented as Paper 4144 at the 39th AIAA Thermophysics Conference, Miami, FL, 25–28 June 2007; received 27 October 2009; revision received 23 January 2010; accepted for publication 31 January 2010.

*Task Manager, Mail Stop ER42, Fluid Dynamics Branch. Senior Member AIAA.
†Project Engineer, Mail Stop EV33, Aerosciences Branch. Member AIAA.
‡Currently Senior Research Fellow, National Space Organization, Hsinchu 30078, Taiwan, ROC. Senior Member AIAA.
§Associate Professor, Department of Mechanical Engineering. Senior Member AIAA.

I. Introduction

NUCLEAR thermal propulsion [1] can carry far larger payloads and reduce travel time for astronauts traveling to Mars than is now possible with chemical propulsion. One of the feasible concepts, extensively tested during the Rover and Nuclear Engine for Rocket Vehicle Application (NERVA) era, is the solid-core concept [2]. It features a solid-core nuclear reactor consisting of hundreds of heat-generating prismatic flow elements, each containing tens of tubular flow channels through which the working fluid, hydrogen, acquires energy and expands in a high-expansion nozzle to generate thrust.

The advantage of using hydrogen as a propellant is well known in the chemical rocket community, due to its low molecular weight. The effect of using hydrogen as a working fluid in a nuclear heat exchanger, however, is not well studied. For example, molecular

hydrogen decomposes to atomic hydrogen during high-temperature heating. Since atomic hydrogen has half the weight of that of molecular hydrogen, it was speculated that the total thrust could be doubled if all of the hydrogen is converted at very high temperatures. In actuality, the hydrogen conversion is probably not uniform across the solid core, since the reactor temperature depends on the hydrogen flow rate distribution and the power profile. In addition, the hydrogen atom could recombine in the nozzle, since temperature decreases rapidly during the gas expansion.

On the other hand, it is always desirable to decrease the reactor weight, and one of the ideas is to reduce the reactor size, which increases the power density. One of the impacts of operating at the combination of high temperature and high power density is a phenomenon known as midsection corrosion, as reported during the legacy engine tests [3], which is the cracking of the coating layer, coupled with an excessive mass loss of the material near the midsection of a flow element. The purpose of the coating layer was to isolate the carbonaceous compound in the flow-element matrix from the attack by hydrogen. The causes of midsection corrosion were speculated as a mismatch in the thermal expansion of flow element and its coating material, high flow-element-web internal-temperature gradients, and change of solid thermal property due to irradiation [3,4].

Moreover, reduction of reactor size often started with reducing the diameter of the flow channels, which results in a higher aspect ratio, or longer flow channels. According to Rayleigh line theory, flow with continuous heat addition in a long tube could choke. When that happens, any further heat addition can only serve to reduce the mass flow rate in the tube or, in other words, to jump to another Rayleigh line of lower mass flow [5]. This could cause unintended mass flow maldistribution, resulting in uneven thermal load in the flow-element matrix and cracking of the coating material. Choking in the heated long flow channel is therefore another possibility causing midsection corrosion.

To better understand the aforementioned design issues, to help the design of the ongoing test apparatus for materials development [4,6], and to aim for the future thrust-chamber design analyses, the objective of this effort is to develop an efficient and accurate multiphysics computational heat transfer methodology that is capable of providing environments for studying those tasks. A unified thermal flowfield of a hypothetical solid-core thrust chamber from the small engine [7] was computed as a first attempt in this effort. The small engine was a *paper engine* designed near the end of the Rover/NERVA era that bears features of most legacy engines tested during that time period, but was never built or tested. By simulating and comparing the computed environments with those of the small-engine design analysis and available test information from other legacy tests, the lessons learned during Rover/NERVA era may be revitalized and a new strategy for reactor design and materials development may be devised.

A two-pronged approach was conducted: a detailed modeling of a single powered flow element that could address the possible causes of the midsection corrosion is reported in a separate effort [8], in which local flow choking in flow channels was computed and analyzed, and a global modeling approach that computes the entire thermal flowfield of the hypothetical small-engine thrust chamber is reported here. The global approach solves the entire thrust chamber with detailed modeling, except the thousands of flow channels in the hundreds of flow elements were lumped together as a porous media, for computational efficiency. The heat transfer between other supporting solid components and the working fluid is solved with the conjugate transfer methodology, which was developed in an earlier effort [4]. The global approach directly links the effect of the distribution of power in the solid core to the ultimate thrust performance. Theoretical power profiles were assumed in place of the neutronics modeling. In total, three sets of theoretical power profiles were assumed and five three-dimensional thrust-chamber computations were performed. Specific impulse, core-exit gas temperature, and pressure drop were computed and compared with those of the hypothetical small engine. Effects of the power profiles on hydrogen conversion, overall heat transfer efficiency, and thrust performance are discussed and reported.

II. Computational Heat Transfer Methodology

A. Fluid Dynamics

The computational methodology was based on a multidimensional, finite volume, viscous, chemically reacting, unstructured grid and pressure-based computational fluid dynamics formulation [9]. Time-varying transport equations of continuity, species continuity, momentum, total enthalpy, turbulent kinetic energy, and turbulent kinetic energy dissipation rate were solved using a time-marching subiteration scheme and are written as

$$\frac{\partial \rho}{\partial t} + \frac{\partial}{\partial x_j}(\rho u_j) = 0 \tag{1}$$

$$\frac{\partial \rho \alpha_i}{\partial t} + \frac{\partial}{\partial x_j}(\rho u_j \alpha_i) = \frac{\partial}{\partial x_j}\left[\left(\rho D + \frac{\mu_t}{\sigma_\alpha}\right)\frac{\partial \alpha_i}{\partial x_j}\right] + \omega_i \tag{2}$$

$$\frac{\partial \rho u_i}{\partial t} + \frac{\partial}{\partial x_j}(\rho u_j u_i) = -\frac{\partial p}{\partial x_i} + \frac{\partial \tau_{ij}}{\partial x_j} \tag{3}$$

$$\begin{aligned}\frac{\partial \rho H}{\partial t} + \frac{\partial}{\partial x_j}(\rho u_j H) &= \frac{\partial p}{\partial t} + Q_r + \frac{\partial}{\partial x_j}\left(\left(\frac{K}{C_p} + \frac{\mu_t}{\sigma_H}\right)\nabla H\right) \\ &+ \frac{\partial}{\partial x_j}\left(\left((\mu + \mu_t) - \left(\frac{K}{C_p} + \frac{\mu_t}{\sigma_H}\right)\right)\nabla\left(\frac{V^2}{2}\right)\right) \\ &+ \frac{\partial}{\partial x_j}\left(\left(\frac{K}{C_p} + \frac{\mu_t}{\sigma_H}\right)\left(u_k\frac{\partial u_j}{\partial x_k} - \frac{2}{3}u_j\frac{\partial u_k}{\partial x_k}\right)\right)\end{aligned} \tag{4}$$

$$\frac{\partial \rho k}{\partial t} + \frac{\partial}{\partial x_j}(\rho u_j k) = \frac{\partial}{\partial x_j}\left[\left(\mu + \frac{\mu_t}{\sigma_k}\right)\frac{\partial k}{\partial x_j}\right] + \rho(\Pi - \varepsilon) \tag{5}$$

$$\begin{aligned}\frac{\partial \rho \varepsilon}{\partial t} + \frac{\partial}{\partial x_j}(\rho u_j \varepsilon) &= \frac{\partial}{\partial x_j}\left[\left(\mu + \frac{\mu_t}{\sigma_\varepsilon}\right)\frac{\partial \varepsilon}{\partial x_j}\right] \\ &+ \rho\frac{\varepsilon}{k}\left(C_1\Pi - C_2\varepsilon + \frac{C_3\Pi^2}{\varepsilon}\right)\end{aligned} \tag{6}$$

A predictor and corrector solution algorithm was employed to provide coupling of the governing equations. A second-order central-difference scheme was employed to discretize the diffusion fluxes and source terms. For the convective terms, a second-order upwind total-variation-diminishing difference scheme was used. To enhance the temporal accuracy, a second-order backward difference scheme was employed to discretize the temporal terms. Details of the numerical algorithm can be found in [8–13].

An extended k-ε turbulence model [14] was used to describe the turbulent flow and turbulent heat transfer. A modified wall function approach was employed to provide wall boundary-layer solutions that are less sensitive to the near-wall grid spacing. Consequently, the model has combined the advantages of both the integrated-to-the-wall approach and the conventional law-of-the-wall approach by incorporating a complete velocity profile and a universal temperature profile [10].

B. Heat Transfer in Solids

The solid heat conduction equation was solved with the gas-side heat flux distributions as its boundary conditions. The solid heat conduction equation can be written as [4]

$$\frac{\partial \rho C_p T_s}{\partial t} = \frac{\partial}{\partial x_j}\left(K\frac{\partial T_s}{\partial x_i}\right) + Q_p + Q_s \tag{7}$$

C. Flow and Heat Transfer in Porous Media

A two-temperature porosity model was formulated with separate thermal conductivities for the flow and the solid parts. The heat transfer between the flow and solid was modeled by using the empirical correlation of heat transfer coefficient for circular pipes as a function of flow Reynolds numbers. Empirical multipliers for both the heat transfer and drag loss were determined by comparing solutions of flow passing through a porous flow element with those of a small-engine 19-channel flow element using detailed conjugate heat transfer modeling [8]. The only affected fluid governing equations are Navier–Stokes and energy equations and can be rewritten as

$$\frac{\partial \rho u_i}{\partial t} + \frac{\partial}{\partial x_j}(\rho u_j u_i) = -\frac{\partial p}{\partial x_i} + \frac{\partial \tau_{ij}}{\partial x_j} - \frac{L}{\beta} \tag{8}$$

$$\begin{aligned}\frac{\partial \rho H}{\partial t} + \frac{\partial}{\partial x_j}(\rho u_j H) &= \frac{\partial p}{\partial t} + Q_r + \frac{\partial}{\partial x_j}\left(\left(\frac{K}{C_p} + \frac{\mu_t}{\sigma_H}\right)\nabla H\right) \\ &+ \frac{\partial}{\partial x_j}\left(\left((\mu + \mu_t) - \left(\frac{K}{C_p} + \frac{\mu_t}{\sigma_H}\right)\right)\nabla\left(\frac{V^2}{2}\right)\right) \\ &+ \frac{\partial}{\partial x_j}\left(\left(\frac{K}{C_p} + \frac{\mu_t}{\sigma_H}\right)\left(u_k\frac{\partial u_j}{\partial x_k} - \frac{2}{3}u_j\frac{\partial u_k}{\partial x_k}\right)\right) + \frac{1}{\beta}Q_s\end{aligned} \tag{9}$$

For the solid heat conduction in porous media,

$$\frac{\partial \rho_s C_{ps} T_s}{\partial t} = \frac{\partial}{\partial x_j}\left(K_s\frac{\partial T_s}{\partial x_i}\right) + \frac{1}{1-\beta}(Q_p - Q_s) \tag{10}$$

For the small-engine 19-channel flow-element heat-exchanger configuration, drag loss in circular pipes can be used as a point of departure. That is,

$$L = \tfrac{1}{2}\rho f_L c_f |U| u_i / d \tag{11}$$

where $c_f = 0.0791 Re^{-0.25}$ is the Blasius formula for turbulent pipe flow [15]. Typical Reynolds numbers in a flow channel range from 10,000 to 40,000.

For the heat-exchange source term,

$$Q_s = \frac{1}{2}\rho f_q \frac{c_f}{p_r^{2/3}}|U|\frac{C_p(T_s - T)}{d} \tag{12}$$

For the purpose of this study, the conjugate heat transfer module for solids was benchmarked with the analysis of a cylindrical specimen heated by an impinging hot hydrogen jet [4]. The computed solid temperature profiles agreed well with those of a standard solid heat transfer code SINDA [16]. The methodology for flow through porous media was verified through a particle-bed nuclear flow element [17] and the space shuttle main engine (SSME) main injector assembly [18]. The numerical and physical models for predicting the thrust and wall heat transfer were benchmarked with an analysis of the SSME thrust-chamber flowfield, in which the computed axial-thrust performance, flow features, and wall heat fluxes compared well with those of the test data [12].

III. Three-Dimensional Thrust-Chamber Modeling

The flow and heat transfer inside a solid-core thrust chamber was modeled after the hypothetical small engine [7]. General geometry and operating conditions were obtained from [7], and certain specific operating conditions and nozzle geometry were provided by the Systems Engineering group.

A. Computational Grid Generation

Hybrid computational grids were generated using a software package GRIDGEN [19]. There are 564 flow elements and 241 support elements, or tie tubes, designed for the solid-core reactor in the small engine. The flow element is shaped like a hexagonal prism, with a length of about 890 mm and a width of about 19 mm from flat to flat [8]. The prismatic flow element contains 19 tubular coolant channels, each with a diameter of about 2.3 mm [8]. Details of the geometry of the flow element can be found in [8]. Each flow element is held in position by three tie tubes and the corresponding hot-end support system (not modeled). The layout of the flow elements and tie tubes of the solid core is such that the whole thrust chamber is symmetrical about a 30 deg pie-shaped section. Grid studies for modeling the physics of major individual components were described in previous publications: e.g., the analysis of a cylindrical specimen heated by an impinging hot hydrogen jet [4], the analysis of flow and heat transfer of a single flow element [8], and the analysis of thrust performance and heat transfer of a rocket engine nozzle [12]. Based on the lessons learned from those studies, a series of grid verification studies using grid sizes of 1,903,278, 1,925,742, 4,681,751, and 7,460,225 points were performed on the nominal case, or case 1. It was found that the computed average pressure drops across the core were very similar and the differences among the computed thrust values were less than 2.5%. Based on those findings and the consideration for computational efficiency, the grid size of 1,925,742 points (or 2,408,198 computational cells) was selected for all the computations. Figure 1 shows a 240 deg view of the computational grid and geometry layout of the thrust-chamber and tie-tube walls. The thrust chamber includes the inlet wall, the pressure vessel, and the nozzle with skirt with expansion ratio of 100. Only tie tubes in the pressure vessel are shown, for clarity. Figure 2 shows a cross-sectional cut of the solid-core computational grid depicting flow elements, tie tubes, slat, and reflector. Note that the 19 channels in each flow element were lumped as one porous flow channel, and the effects of that were modeled with Eqs. (8–12).

B. Thermal Properties and Kinetics

Real gas thermodynamic properties were obtained from [20]. These properties were generated for temperatures up to 20,000 K. The peak gas temperature computed did not exceed 10,000 K and hence is well within the applicable range. A two-species, two-reaction chemical kinetics mechanism was used to describe the finite

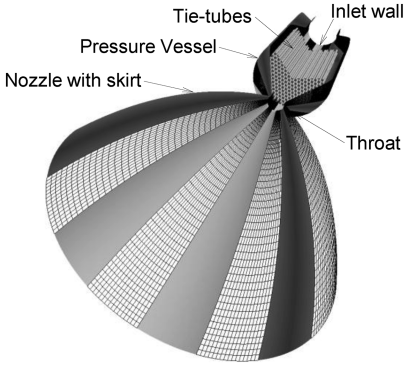

Fig. 1 Computational grid and geometry representation of the solid-core small-engine thrust chamber.

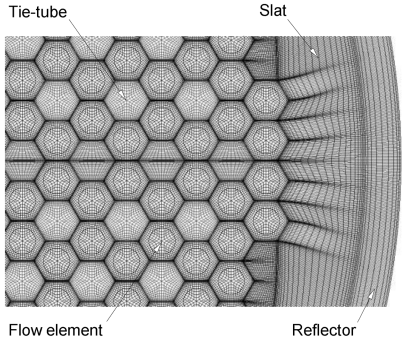

Fig. 2 Cross-sectional computational grid layout for the solid core of the small engine. For illustration, circles are imposed onto the flow elements to differentiate them from the tie tubes.

Table 1 Hydrogen reaction kinetics mechanism

Reaction[a]	A	B	E/R	M	Ref.
$M + H + H = H_2 + M$	5.0E15	0	0	H_2, H	[21]
$M + H_2 \rightarrow H + H + M$	8.8E14	0	48,300	H_2	[22]

[a]M is third-body collision partner and rate constant $K = AT^B \exp(-E/RT)$.

Table 2 Run matrix

Case	Axial power shape	Radial power shape	Chemistry
1	Cosine	Cosine	Finite rate
2	Cosine	Cosine	Frozen
3	Clipped cosine	Flattened	Finite rate
4	Clipped cosine	Flattened	Frozen
5	Clipped cosine	Flat	Finite rate

rate hydrogen dissociation and recombination reactions, as shown in Table 1. The first hydrogen recombination reaction is abridged from a large set of mechanisms for kerosene combustion [21], and an irreversible second reaction [22] is added to describe the hydrogen decomposition. The kinetics of the first hydrogen recombination have been benchmarked through many kinetic mechanism studies, as described in [21], and the kinetic rates of the second hydrogen recombination reaction were measured [22]. Note that the first reaction is a reversible reaction.

Solid-core flow-element material is assumed to be the (U, Zr)C-graphite composite A, which was tested as flow-element material in a legacy reactor. Properties of thermal conductivity, density, and heat capacity as a function of temperature were obtained for (U, Zr)C-graphite composite A from [4]. Those properties [23] of beryllium were used for the reflector and slat. The slat acts as a buffer between the core and the reflector.

C. Boundary, Inlet Conditions, and Run Matrix

A no-slip boundary condition was applied to all solid walls, and a supersonic outflow boundary condition was employed at the nozzle exit. A fixed total pressure and temperature condition was used at the inlet. Inlet hydrogen flow properties were obtained from a system model simulation. Since the minor thermal effects of tie tubes were included in the system model simulation, an adiabatic-wall boundary condition was used for tie-tube walls in lieu of modeling the heat transfer inside the tie tubes. The core surrounding components such as the slat and reflector were treated as heat-conducting solids to provide accurate boundary conditions for the solid-core boundary. The heat conducted from the core through the slat and reflector to the outer thrust-chamber walls was dissipated to a far-field temperature assumed to be 310 K.

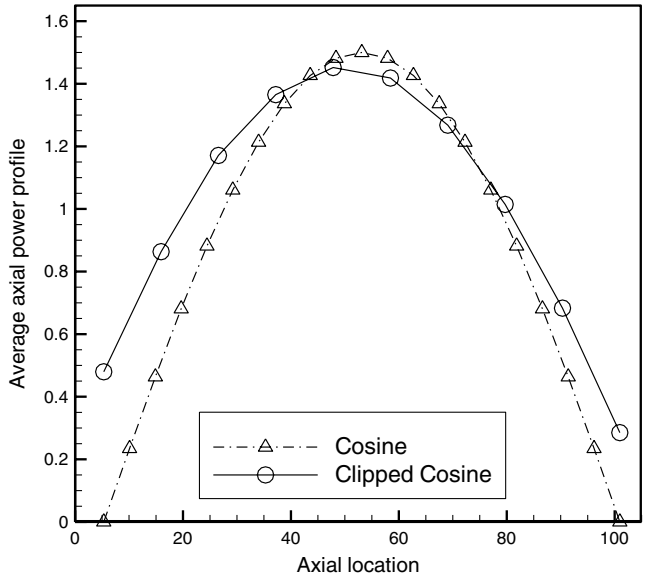

Fig. 3 Power profiles used in the axial direction.

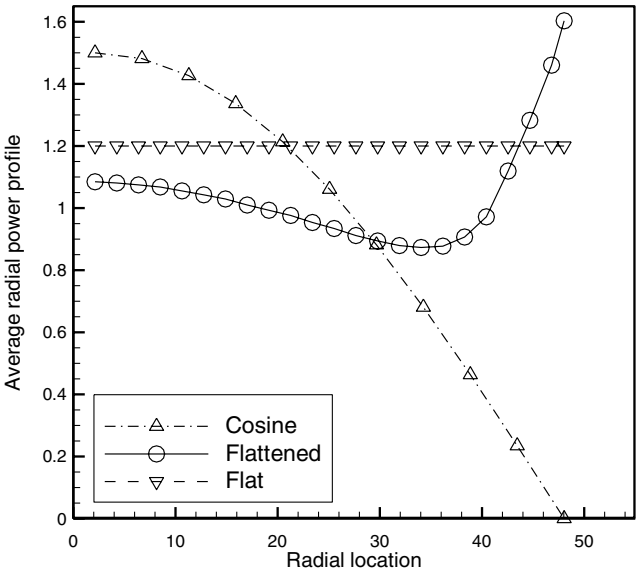

Fig. 4 Power profiles employed in the radial direction.

Power profiles were imposed onto the solid-core domain in lieu of the neutronics calculations. Two axial and three radial power profiles were used to show the effect on the heat transfer and thrust performance, as shown in Figs. 3 and 4. The run matrix is formed with three combinations of these power profiles, as shown in Table 2. The first combination uses the shape of a cosine curve in both the axial and radial directions, which resembles the thermal flux distribution in bare reactors [23], and is simply named as the cosine–cosine power profile. By definition, the power of the cosine–cosine power profile peaks at the middle of the core and drops to zero at the core boundary, due to escaping neutrons. The second combination is prescribed by a neutronics calculation with varied uranium loading. It gives a clipped cosine profile in the axial direction and a flattened profile in the radial direction and is dubbed as the clipped cosine-flattened power profile. The varied fuel loading flattens the power profile in the radial direction, but the power rises near the boundary to show the effect of the reflector, as shown in Fig. 4. The idea of flattening the radial profile is such that the flow in the channels is heated more uniformly, thereby improving the heat transfer efficiency. It is assumed that the clipped cosine-flattened profile is the closest power profile to that intended for the small engine. To study the effect of a theoretically flat radial power distribution, which may be achieved with a combination of varied fuel loading and working fluid flow distribution, the third combination employs the clipped cosine curve in the axial direction and a flat curve in the radial direction, which is called the clipped cosine-flat power profile.

In total, five cases were computed in this study, as shown in Table 2. To further understand the effect of chemistry options on hydrogen conversion, heat transfer and thrust performance, finite rate, and frozen chemistries were applied to the cosine–cosine power profile separately as cases 1 and 2 and were applied to the clipped cosine-flattened power distribution as cases 3 and 4. Finite rate chemistry means that the hydrogen decomposition and recombination reactions were invoked and the reaction rate was finite, as shown in Table 1. When finite rate chemistry is used, the species composition is a function of the local temperature, pressure, and residence time. Frozen chemistry means that the inlet composition is frozen and transported downstream, with chemical reactions deactivated.

IV. Results and Discussion

A. Case 1: Cosine–Cosine Power Profile, Finite Rate Chemistry

Figure 5 shows the computed thrust-chamber temperatures and hydrogen-atom mass-fraction contours for the cosine–cosine power

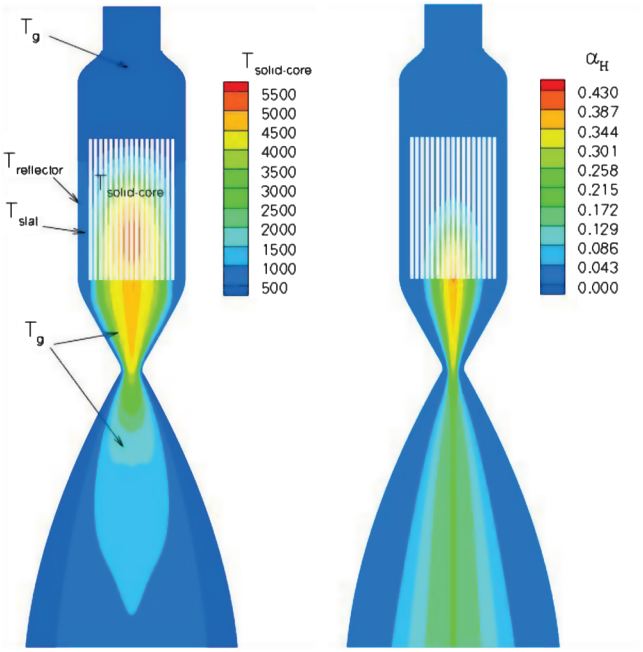

Fig. 5 Solid and gas temperatures and hydrogen-atom mass-fraction contours on the symmetry plane for case 1.

distribution with finite-rate-chemistry case. In the temperature contours plot, those in the solid core represent the solid temperatures in the flow elements, the portions surrounding the solid core depict the temperatures in the slat and reflector, and the rest are the gas temperature contours. It can be seen that the solid-core temperature contours reflect the cosine–cosine power distribution with a heat transfer delay in the axial direction. The hydrogen-gas temperature contours in the solid core (not shown) take the same shape as those of the solid temperature, except lower. The heat transfer delay in the axial direction is a result of the energy balance between the cooling from the incoming cold hydrogen in the flow channels and the heating from the nuclear material in the web of the flow elements. It is apparent that the effect of cold hydrogen pushes the peak flow-element temperature downstream. The hydrogen-atom contours also look similar to those of the solid-core temperature contours, with the peak conversion pushed to near the end of the core, due to the same effect that pushed the peak solid temperature away from the center core. In short, coolant hydrogen enters the thrust chamber at about 370 K, heats up to about 4800 K in the solid core, then cools and expands into the diverging nozzle to generate the thrust. Molecular hydrogen decomposes to atomic hydrogen at about 2400 K, and hence most of the hydrogen atoms are formed while in the flow elements. Once the local temperature starts to cool, i.e., during the expansion in the nozzle, hydrogen atoms recombine to become molecular hydrogen. The peak hydrogen-atom mass fraction in case 1 is 0.40, or 40% conversion.

Figure 6 shows the computed solid and gas axial temperature profiles on the symmetry plane, along with the centerline of each flow element. Only the temperature profiles for the first, third, fifth, seventh, and ninth flow elements from the center tie tube are plotted, for clarity. The solid temperatures (shown as dashed lines) lead those of the gas temperatures (solid lines), showing the effect of the heat transfer coefficient between the flow element and gas. The gas temperatures appear to peak near the core exit, and the solid temperatures appear to peak earlier for the first, third, and fifth fuel elements, but not for the seventh and ninth fuel elements. The lead decreases at the seventh flow element and disappears completely at the ninth flow element. These axial temperature profiles reflect the effect of the cosine–cosine power profile that concentrates the power in the middle of the core and drops to zero at the core boundary. The peak solid temperature for the ninth flow element is the lowest at around 700 K. The gas core-exit temperature is about 4600 K at the first flow element and is again about 700 K at the ninth flow element. The 3900 K temperature spread indicates a very nonuniform temperature distribution at the core exit, or poor heat transfer efficiency, caused by the cosine–cosine power distribution. Note that the temperature gradient of the solid temperature is very steep for the first flow element occurring at a location between the core entrance and the peak temperature, indicating that the midsection corrosion could have happened over here.

B. Case 2: Cosine–Cosine Power Profile, Frozen Chemistry

Frozen chemistry means that the entering coolant hydrogen composition is frozen and that the molecular hydrogen decomposition is not allowed and a hydrogen atom is not formed. As a result, the temperatures of the frozen-chemistry case are much higher than those of the finite-rate-chemistry case, because the hydrogen decomposition reaction is endothermic. That is, substantial heat was used to decompose molecular hydrogen into the atomic hydrogen in the finite-rate-chemistry case. The frozen-chemistry case is obviously theoretical and its high solid and gas temperatures are not physical, since hydrogen decomposition occurs naturally. The frozen-chemistry case, though, demonstrates that the inclusion

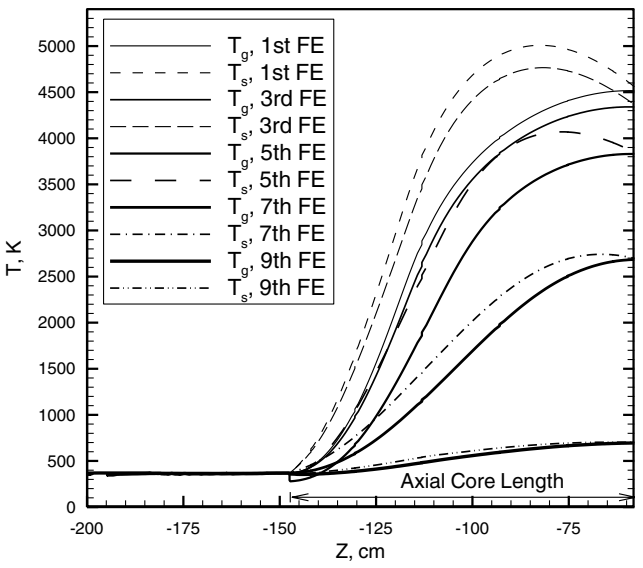

Fig. 6 Solid and gas axial temperature profiles for the first, third, fifth, seventh, and ninth flow elements (FE) on the symmetry plane for case 1.

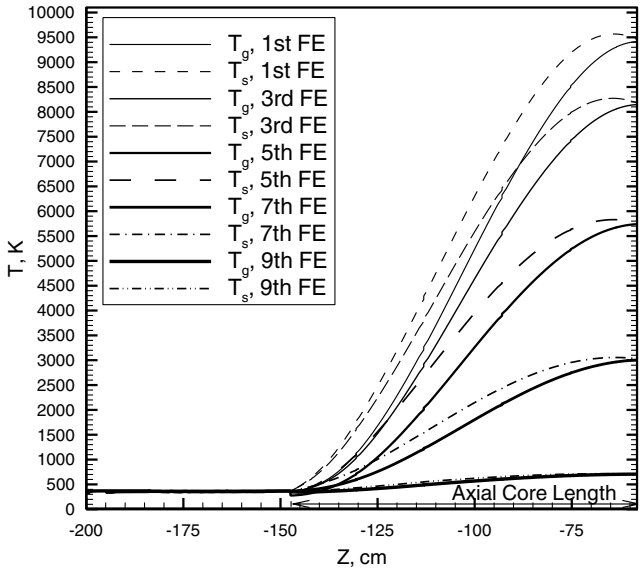

Fig. 7 Solid and gas axial temperature profiles for the first, third, fifth, seventh, and ninth flow elements on the symmetry plane for case 2.

of finite-rate-chemistry calculation is important in getting the proper energy balance and hence the correct temperature predictions.

Figure 7 shows the computed solid and gas axial temperature profiles for the first, third, fifth, seventh, and ninth flow elements on the symmetry plane for the cosine–cosine power distribution with frozen-chemistry case. The peak core-exit gas temperature at the first flow element is about 9400 K and that for the ninth flow element is about 650 K. The gas temperature spread at the core exit is therefore about 8750 K, much larger than the 3900 K of the finite-rate-chemistry case. This is again not physical, since hydrogen decomposition occurs naturally whenever the gas temperature exceeds 2400 K.

C. Case 3: Clipped Cosine-Flattened Power Profile, Finite Rate Chemistry

It is obvious that the cosine–cosine power distribution not only causes peak solid temperatures that are too high, but also the very nonuniform core-exit gas temperatures, indicating inefficient heat transfer. Fortunately, by measures such as varying the fuel loading, a flattened distribution in the radial direction could be achieved, as shown in Fig. 4. Note that this profile is not completely flat, since the normalized power is at about 1.1 in the middle, drops to a minimum at about 0.9, and rises to a maximum of 1.6 at the boundary, but compared with the nominal cosine power profile, it is relatively flat. In fact, by our best estimation, this clipped cosine (in the axial direction) flattened (in the radial direction) power profile is probably the most representative of that intended for the small engine. Figure 8 shows the computed solid and gas temperatures and hydrogen-atom mass-fraction contours for this clipped cosine-flattened power profile with finite-rate-chemistry case. It can be seen that the solid and gas temperature contours and the atomic-hydrogen contours reflect the effect of the clipped cosine-flattened power distribution shown in Figs. 3 and 4. Compared with the temperature contours in Fig. 5, those in Fig. 8 are more uniform. The peak solid and gas temperatures in Fig. 8 at about 3149 and 3081 K, respectively, are much lower than those in Fig. 5 at 5369 and 4596 K, respectively. As a result, the peak hydrogen-atom mass fraction also drops from a high 0.40 in Fig. 5 to a low 0.02, or a 2% conversion. Note that the atomic-hydrogen contours exhibit a more pronounced striation in the pressure vessel beneath the core than those in case 1. This is caused by the higher power profile at the core boundary, resulting in higher temperature at the boundary, which promotes more local hydrogen conversion than that of case 1.

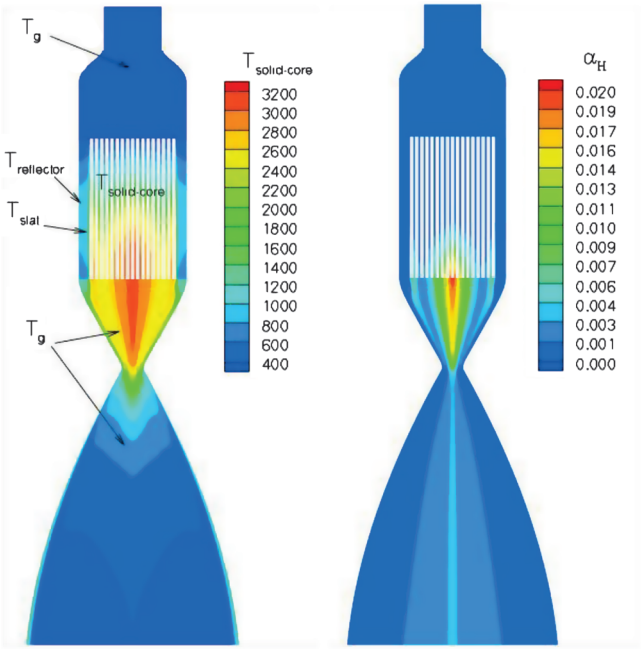

Fig. 8 Solid and gas temperatures and hydrogen-atom mass-fraction contours on the symmetry plane for case 3.

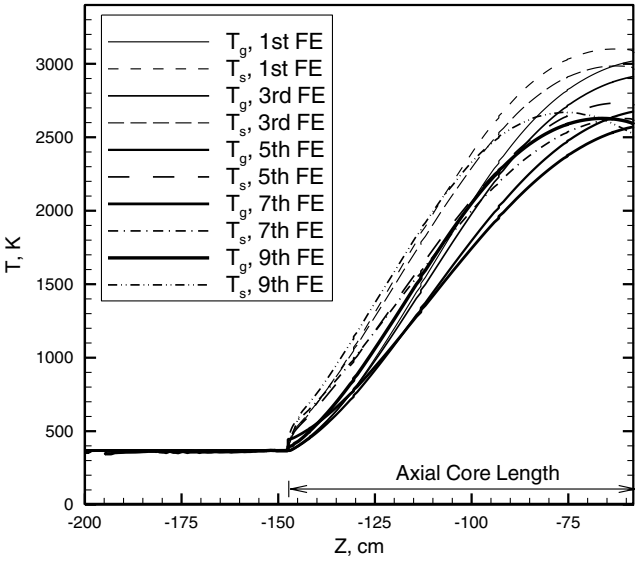

Fig. 9 Solid and gas axial temperature profiles for the first, third, fifth, seventh, and ninth flow elements on the symmetry plane for case 3.

Figure 9 shows the computed solid and gas axial temperature profiles on the symmetry plane. Compared with those in Fig. 6, it can be seen that other than the ninth element, the solid temperature generally only leads the gas temperature slightly, because the flattened radial power profile is more uniform than the nominal cosine profile used for Fig. 6. The peak core-exit gas temperature at the first fuel element is about 3037 K and that at the ninth fuel element is about 2514 K. The temperature spread of the gas temperature at the core exit is hence only about 523 K, much less than that of 3900 K in case 1, indicating that the gas core-exit temperature of case 3 is much more uniform than that of case 1. The flattened radial power profile is therefore an improvement over the cosine power distribution.

Note that it is possible to physically flatten the flattened radial power profile of Fig. 4 even more, with further fine tuning of the fuel loading. In addition, the hydrogen mass flow may be profiled similarly to the radial power profile. That way, the mass flow rates at locations of higher power will be high and those at locations of lower power will be low. The result is an even more uniform core-exit gas temperature distribution than that in case 3, such as the flat radial

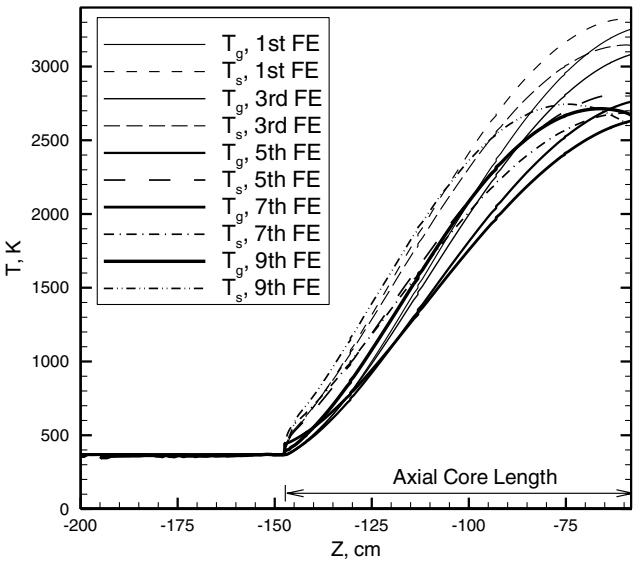

Fig. 10 Solid and gas axial temperature profiles for the first, third, fifth, seventh, and ninth flow elements on the symmetry plane for case 4.

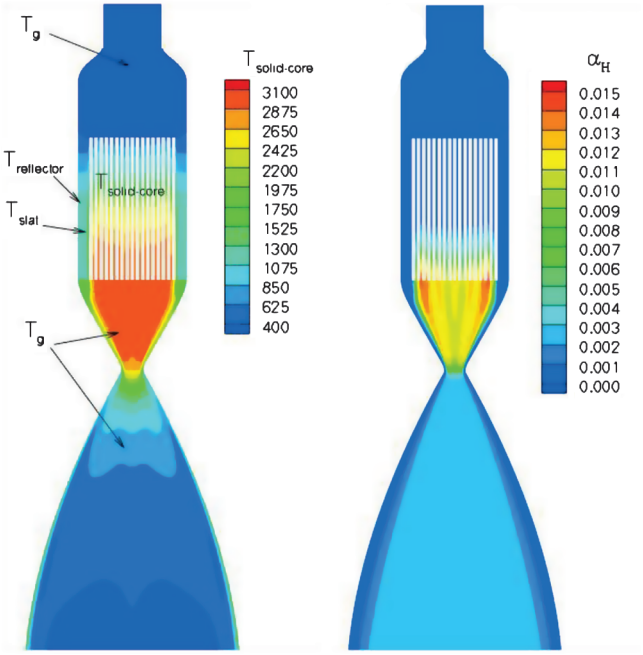

Fig. 11 Solid and gas temperatures and hydrogen-atom mass-fraction contours on the symmetry plane for case 5.

power profile in case 5. The mass flow profiling may be physically achieved with the installation of various sizes of orifices at the entrance of each flow element. The effect of mass flow profiling may also be numerically modeled with the current modeling technique but is out of the scope of this task.

D. Case 4: Clipped Cosine-Flattened Power Profile, Frozen Chemistry

Figure 10 shows the computed solid and gas axial temperature profiles on the symmetry plane for case 4. The depictions for the temperature profiles in Fig. 10 are very similar to those of Fig. 9, except the peak temperatures and the temperature spread are slightly higher, due to the frozen chemistry. The reason why the temperature differences between case 3 and case 4 are much smaller than those of case 1 and case 2 is because of the power distributions. The effect of frozen chemistry is more pronounced with the nonuniform cosine–cosine power profile than with the more uniform clipped cosine-flattened power profile.

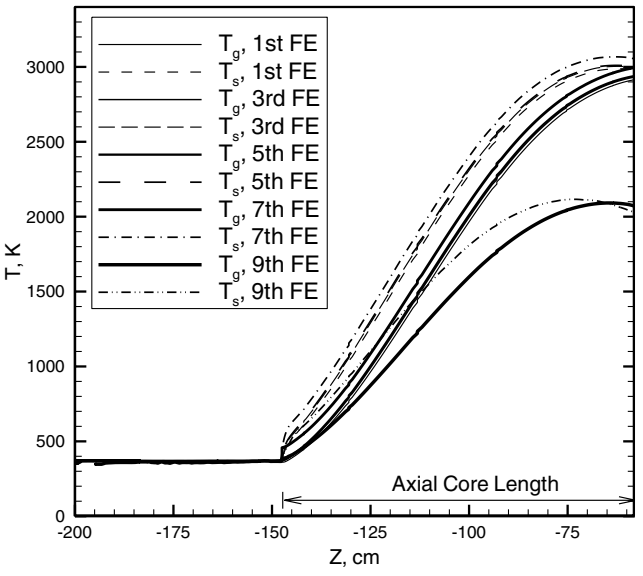

Fig. 12 Solid and gas axial temperature profiles for the first, third, fifth, seventh, and ninth flow elements on the symmetry plane for case 5.

E. Case 5: Clipped Cosine-Flat Power Profile, Finite Rate Chemistry

Case 5 uses the clipped cosine profile for the axial power distribution and a flat profile for the radial power distribution. The resulting temperature and hydrogen mass-fraction contours are shown in Fig. 11. It can be seen in terms of the solid-core radial temperature distribution and the uniformity of the gas temperature beneath the solid core that this one is the most uniform and so are the hydrogen mass-fraction contours. Note that the hydrogen-atom conversion is only about 1.5%.

Figure 12 shows the solid and gas axial temperature profiles for the first, third, fifth, seventh, and ninth flow elements in the solid core. It can be seen that the temperature spreads among the first, third, fifth and seventh flow elements are much smaller than those of earlier cases, except those of the ninth flow element, due to the heat loss to the slat and reflector. From Figs. 11 and 12, it can be seen this flat radial power profile is a very good power profile in terms of general uniformity of the temperatures for both solid and gas temperatures inside the core and for gas exit temperatures.

F. Summary

Table 3 shows a summary of the computed heat transfer and thrust performance parameters for all five cases. The second column shows the averaged core-exit gas temperatures. These were obtained by averaging the temperatures at the core exit for all nine elements on the symmetry plane. It can be seen that the averaged core-exit gas temperatures for the cosine–cosine power distribution cases are much higher than the small-engine design temperature of 2750 K, and the temperature of the frozen-chemistry case at 5514 K is much higher that of the finite-rate-chemistry case at 3334 K. The averaged core-exit temperatures of the clipped cosine-flattened power distribution cases are much lower, with 2785 K for the finite-rate-chemistry case and 2927 K for the frozen-chemistry case. As mentioned before, the hydrogen decomposition is endothermic, and hence the temperatures of the frozen-chemistry case are higher than those of the finite-rate-chemistry case. And again, since hydrogen decomposition is naturally occurring at high temperatures, the results for the frozen-chemistry cases are unphysical but demonstrated the importance of including the finite-rate-chemistry calculation for accurate temperature predictions. As for case 5, its averaged core-exit gas temperature at 2782 K is the closest to that of the small-engine design value.

The third column shows the temperature spread, or the difference of the core-exit gas temperature between the first and the ninth flow elements. Lower spread represents more uniform temperature distribution among the flow elements, or better heat transfer efficiency. It can be seen that the more uniform clipped cosine-flattened power profile produces much better heat transfer efficiency than that of the cosine–cosine power distribution. For example, the temperature spread of 523 K of case 3 is much less than that of 3900 K of case 1. Again, the effect of frozen chemistry results in higher spread than that of the finite rate chemistry, which is not physical. Note that although the temperature spread of case 5 at 842 K is higher than those of cases 3 and 4, it is actually more uniform in most of the core, except at the ninth flow element.

The fourth column shows the computed specific impulses. Remember that the maximum atomic-hydrogen mass fraction is 0.4 for case 1, 0.02 for case 3, and 0.015 for case 5, yet the I_{sp} of case 5 is higher than that of case 3, which in turn is higher than that of case 1.

Table 3 Summary of the heat transfer and performance parameters

Case	$T_{g,\text{core exit}}$, K	$\Delta T_{g,\text{core exit}}$, K	I_{sp}	ΔP_{core}, atm	$T_{s,\max}$
1	3334	3900	811	8.9	5369
2	5514	8750	844	8.9	9366
3	2785	523	868	9.1	3149
4	2927	654	873	9.1	3365
5	2782	842	900	9.1	3066
Small engine	2750	——	860–875	9.0	——

These results demonstrated that the notion of higher temperature, more atomic hydrogen, and therefore higher thrust is not likely true. Rather, based on a fixed power, it is the more uniform power profile that produces the higher thrust. The fifth column shows the comparison of the computed core pressure drops. It can be seen that all are close to the design value of 9 atm, although those of the cosine–cosine power distribution are slightly lower. The last column shows the computed peak solid temperatures. It can be seen that the lowest peak solid temperature belongs to case 5 and the reason is clear.

As mentioned before, we have designed the clipped cosine-flattened power profiles to match those intended for the design of the paper engine: the small engine, to the best of our knowledge. As a result, the computed averaged core-exit gas temperature, specific impulse, and core pressure drop of case 3 agree very well with those of the design values, indicating that the simulation with the computational model developed in this work closely simulated the fluid, thermal, and hydrogen environments in the original small-engine design. That result satisfies part of the goal of the entire effort as described in [1–4]: i.e., to recover what has been lost in the legacy programs using current technology and to develop better designs or materials for the future missions. The latter part of that goal is demonstrated in the result of case 5, in which the computed averaged core-exit gas temperature and core pressure drop are equally as good as those of case 3, yet its I_{sp} is 32 s higher than that of case 3, demonstrating that the methodology developed in this work can be used to help guide the direction of the design: i.e., more uniform radial power distribution generates higher heat transfer efficiency, lower peak solid temperature, and higher thrust performance.

V. Conclusions

A multiphysics computational heat transfer methodology was developed to predict heat transfer efficiency and thrust performance for a virtual-solid-core nuclear thermal engine thrust chamber: the small engine. The methodology computes a unified thrust-chamber thermal flowfield constituting the inlet plenum, the pressure vessel, and the nozzle. Multiphysics invoked include the turbulent flow and heat transfer, finite rate chemistry, power generation, and conjugate heat transfer for solids and porous media. The computed result of the core-exit gas temperature, core pressure drop, and specific impulse for the clipped cosine-flattened power profile agree with the virtual engine design very well. Finite rate chemistry is found to be very important in predicting the proper energy balance, because naturally occurring hydrogen decomposition is endothermic. In addition, high hydrogen conversion neither improves the heat transfer efficiency nor increases the thrust performance. Rather, it is the more uniform power profile that produces lower peak solid temperature, higher heat transfer efficiency, and higher thrust performance.

Acknowledgments

This study was partially supported by a Nuclear Systems Office task entitled "Multiphysics Thrust Chamber Modeling" with funding from the Prometheus Power and Propulsion Office, NASA headquarters. Ron Porter was the NASA Marshall Space Flight Center Nuclear Systems Office Manager. Wayne Bordelon was the Nuclear Thermal Propulsion Manager. Michael Houts was the Nuclear Research Manager. Steve Simpson and Karl Nelson provided the clipped cosine-flattened power profile, nozzle geometry, and system modeling results. Bill Emrich suggested the cosine–cosine power profile. Jeff Lin debugged the porosity drag calculation. Solid material thermal properties provided by Panda Binayak, Robert Hickman, and Bill Emrich are also acknowledged.

References

[1] Bordelon, W. J., Ballard, R. O., and Gerrish, H. P., Jr., "A Programmatic and Engineering Approach to the Development of a Nuclear Thermal Rocket for Space Exploration," AIAA Paper 2006-5082, July 2006.

[2] Howe, S. D., "Identification of Archived Design Information for Small Class Nuclear Rockets," 41st AIAA/ASME/SAE/ASEE Joint Propulsion Conference, AIAA Paper 2005-3762, Tucson, AZ, 2005.

[3] Emrich, W. J., Jr., "Non-Nuclear NTR Environment Simulator," *Space Technology and Applications International Forum (STAIF-2006)*, edited by El-Genk, M. S., Melville, N. Y., AIP Proceedings, Vol. 813, American Inst. of Physics, Melville, NY, Feb. 2006, pp. 531–536.

[4] Wang, T.-S., Luong, V., Foote, J., Litchford, R., and Chen, Y.-S., "Analysis of a Cylindrical Specimen Heated by an Impinging Hot Hydrogen Jet," *9th AIAA/ASME Joint Thermophysics and Heat Transfer Conference*, AIAA Paper 2006-2926, San Francisco, CA, 2006.

[5] James, E. A. J., *Gas Dynamics*, Allyn and Bacon, Boston, 1969.

[6] Wang, T.-S., Foote, J., and Litchford, R., "Multiphysics ThermalFluid Design Analysis of a Non-Nuclear Tester for Hot-Hydrogen Material Development," *Space Technology and Applications International Forum (STAIF-2006)*, edited by El-Genk, M. S., and Melville, N. Y., AIP Proceedings, Vol. 813, American Inst. of Physics, Melville, NY, Feb. 2006, pp. 537–544.

[7] Durham, F. P., "Nuclear Engine Definition Study," Vol. 1, Los Alamos National Lab., Rept. LA-5044-MS, Los Alamos, NM, Sept. 1972.

[8] Cheng, G., Ito, Y., Ross, D., Chen, Y.-S., and Wang, T.-S., "Numerical Simulations of Single Flow Element in a Nuclear Thermal Thrust Chamber," 39th AIAA Thermophysics Conference, AIAA Paper 2007-4143, Miami, FL, 2007.

[9] Shang, H. M., and Chen, Y.-S., "Unstructured Adaptive Grid Method for Reacting Flow Computation," AIAA Paper 1997-3183, Seattle, WA, 1997.

[10] Wang, T.-S., Droege, A., D'Agostino, M., Lee, Y.-C., and Williams, R., "Asymmetric Base-Bleed Effect on Aerospike Plume-Induced Base-Heating Environment," *Journal of Propulsion and Power*, Vol. 20, No. 3, 2004, pp. 385–393. doi:10.2514/1.10385

[11] Wang, T.-S., Chen, Y.-S., Liu, J., Myrabo, L. N., and Mead, F. B., Jr., "Advanced Performance Modeling of Experimental Laser Lightcraft," *Journal of Propulsion and Power*, Vol. 18, No. 6, 2002, pp. 1129–1138. doi:10.2514/2.6054

[12] Wang, T.-S., "Multidimensional Unstructured-Grid Liquid Rocket Engine Nozzle Performance and Heat Transfer Analysis," *Journal of Propulsion and Power*, Vol. 22, No. 1, 2006, pp. 78–84. doi:10.2514/1.14699

[13] Wang, T.-S., "Transient Three-Dimensional Startup Side Load Analysis of a Regeneratively Cooled Nozzle," *Shock Waves*, Vol. 19, No. 3, 2009, pp. 251–264. doi:10.1007/s00193-009-0201-2

[14] Chen, Y.-S., and Kim, S. W., "Computation of Turbulent Flows Using an Extended k-ε Turbulence Closure Model," NASA CR-179204, 1987.

[15] Bird, R. B., Stewart, W. E., and Lightfoot, E. N., *Transport Phenomena*, Wiley, New York, 1960.

[16] Gaski, J., "The Systems Improved Numerical Differencing Analyzer (SINDA) Code—A User's Manual," Aerospace Corp., El Segundo, CA, Feb. 1986.

[17] Wang, T.-S., and Schutzenhofer, L. A., "Numerical Analysis of a Nuclear Fuel Element for Nuclear Thermal Propulsion," AIAA Paper 91-3576, Sept., 1991.

[18] Cheng, G.-C., Chen, Y.-S., and Wang, T.-S., "Flow Distribution Around the SSME Main Injector Assembly Using Porosity Formulation," AIAA Paper 95-0350, Jan. 1995.

[19] Steinbrenner, J. P., Chawner, J. R., and Fouts, C., "Multiple Block Grid Generation in the interactive Environment," AIAA Paper 90-1602, June 1990.

[20] McBride, B. J., Zehe, M. J., and Gordon, S., "NASA Glenn Coefficients for Calculating Thermodynamic Properties of Individual Species," NASA John H. Glenn Research Center at Lewis Field, TP-2002-211556, Cleveland, OH, Sept. 2002.

[21] Wang, T.-S., "Thermophysics Characterization of Kerosene Combustion," *Journal of Thermophysics and Heat Transfer*, Vol. 15, No. 2, 2001, pp. 140–147. doi:10.2514/2.6602

[22] Baulch, D. L., Drysdale, D. D., Horne, D. G., and LLoyd, A. C., *Evaluated Kinetic Data for High temperature Reactions*, Vol. 1, Chemical Rubber Co., Cleveland, Ohio, 1972.

[23] Glasstone, S., and Edlund, M. C., *The Elements of Nuclear Reactor Theory*, D. Van Nostrand, Toronto, 1958.

K. Frendi
Associate Editor